



HAL
open science

Mechanical properties and processes of deformation in shallow sedimentary rocks from subduction zones: an experimental study

Leslie Gadenne, Hugues Raimbourg, Rémi Champallier, Yuzuru Yamamoto

► **To cite this version:**

Leslie Gadenne, Hugues Raimbourg, Rémi Champallier, Yuzuru Yamamoto. Mechanical properties and processes of deformation in shallow sedimentary rocks from subduction zones: an experimental study. *Geochemistry, Geophysics, Geosystems*, 2014, 15 (12), pp.5001-5014. 10.1002/2014GC005580 . insu-01097223

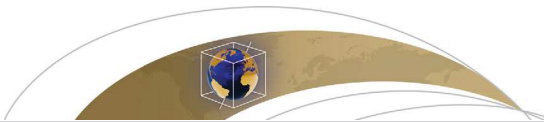
HAL Id: insu-01097223

<https://insu.hal.science/insu-01097223>

Submitted on 12 Jan 2015

HAL is a multi-disciplinary open access archive for the deposit and dissemination of scientific research documents, whether they are published or not. The documents may come from teaching and research institutions in France or abroad, or from public or private research centers.

L'archive ouverte pluridisciplinaire **HAL**, est destinée au dépôt et à la diffusion de documents scientifiques de niveau recherche, publiés ou non, émanant des établissements d'enseignement et de recherche français ou étrangers, des laboratoires publics ou privés.



RESEARCH ARTICLE

10.1002/2014GC005580

Mechanical properties and processes of deformation in shallow sedimentary rocks from subduction zones: An experimental study

Key Points:

- Deformation operates by compaction-assisted shearing and faulting
- Cement breakage induces a decrease in poroelastic stiffness
- V_p anomalies could be induced by cement breakage/microcracks opening

Supporting Information:

- Supporting Information

Correspondence to:

L. Gadenne,
leslie.gadenne@univ-orleans.fr

Citation:

Gadenne, L., H. Raimbourg, R. Champallier, and Y. Yamamoto (2014), Mechanical properties and processes of deformation in shallow sedimentary rocks from subduction zones: An experimental study, *Geochem. Geophys. Geosyst.*, 15, doi:10.1002/2014GC005580.

Received 19 SEP 2014

Accepted 8 DEC 2014

Accepted article online 13 DEC 2014

Leslie Gadenne^{1,2,3}, Hugues Raimbourg^{1,2,3}, Rémi Champallier^{1,2,3}, and Yuzuru Yamamoto⁴

¹Institut des Sciences de la Terre d'Orléans, Univ d'Orléans, UMR 7327, Orléans, France, ²CNRS/INSU, Institut des Sciences de la Terre d'Orléans, UMR 7327, Orléans, France, ³BRGM, Institut des Sciences de la Terre d'Orléans, UMR 7327, BP 36009, Orléans, France, ⁴Institute for Research on Earth Evolution, JAMSTEC, Yokosuka, Japan

Abstract To better constrain the mechanical behavior of sediments accreted to accretionary prism, we conducted triaxial mechanical tests on natural samples from the Miura-Boso paleo-accretionary prism (Japan) in drained conditions with confining pressures up to 200 MPa as well as postexperiments P-wave velocity (V_p) measurements. During experiments, deformation is principally noncoaxial and accommodated by two successive modes of deformation, both associated with strain-hardening and velocity-strengthening behavior: (1) compaction-assisted shearing, distributed in a several mm-wide shear zone and (2) faulting, localized within a few tens of μm -wide, dilatant fault zone. Deformation is also associated with (1) a decrease in Young's modulus all over the tests, (2) anomalously low V_p in the deformed samples compared to their porosity and (3) an increase in sensitivity of V_p to effective pressure. We interpret this evolution of the poroelastic properties of the material as reflecting the progressive breakage of intergrain cement and the formation of microcracks along with macroscopic deformation. When applied to natural conditions, these results suggest that the deformation style (localized versus distributed) of shallow ($z < \text{a few km}$) sediments is mainly controlled by the variations in stress/strain rate during the seismic cycle and is therefore independent of the porosity of sediments. Finally, we show that the effect of strain, through cement breakage and microcracks formation, may lower V_p for effective pressure up to 40 MPa. As a consequence, the low V_p anomalies observed in Nankai accretionary prisms by seismic imaging between 2 and 4 km depth could reflect sediment deformation rather than porosity anomalies.

1. Introduction

Recently, several studies have shown that the underthrust section of the Nankai subduction zone, is characterized by low seismic impedance [Bangs and Shipley, 1999; Park et al., 2002; Bangs et al., 2009]. Similarly, a recent study made by Kitajima and Saffer [2012] reports two broad regions of low seismic velocity along the Nankai subduction plate boundary megathrust offshore SW Japan (between 2 and 4 km and at 10 km below the seafloor). Low seismic velocity/impedance is commonly interpreted as reflecting high porosity of sediments with respect to the surrounding sediments [Erickson and Jarrard, 1998; Hoffman and Tobin, 2004]. This reasoning is based on the simplifying hypothesis that, for a given sediment lithology, velocity converts into porosity, which itself is a function of effective pressure/pore fluid pressure [Karig, 1996]. Indeed, many studies have aimed at deriving empirical relationships between velocity and porosity [Wyllie et al., 1958; Raymer et al., 1980; Han et al., 1986; Issler, 1992; Erickson and Jarrard, 1998], while the conversion of porosity into fluid pressure is based on compaction laws [Bray and Karig, 1985; Karig, 1996]. These laws are built in deep basin settings, where there is limited tectonics and sediment compaction results simply from vertical, uniaxial loading. As a consequence, these laws may apply for underthrusting sediment beneath a mechanically weak décollement [e.g., Byrne and Fisher, 1990] but their relevance to sediments strongly tectonized above the décollement is questionable. Within the accretionary prism, compaction meant as pore volume collapse is not governed simply by uniaxial compaction laws [Le Pichon et al., 1990; Saffer, 2003; Saffer and Bekins, 2006] but it proceeds also for a large part from horizontal compression [Hunze and Wonik, 2007]. Furthermore, beyond the macroscopic porosity decrease, the modes of deformation in accreted sediments are indeed multifold, as attested by natural examples from the shallow portion of accretionary prisms, exhumed in fossil subduction zones such as the Boso Peninsula, Japan [Yamamoto et al., 2005]. There, deformation

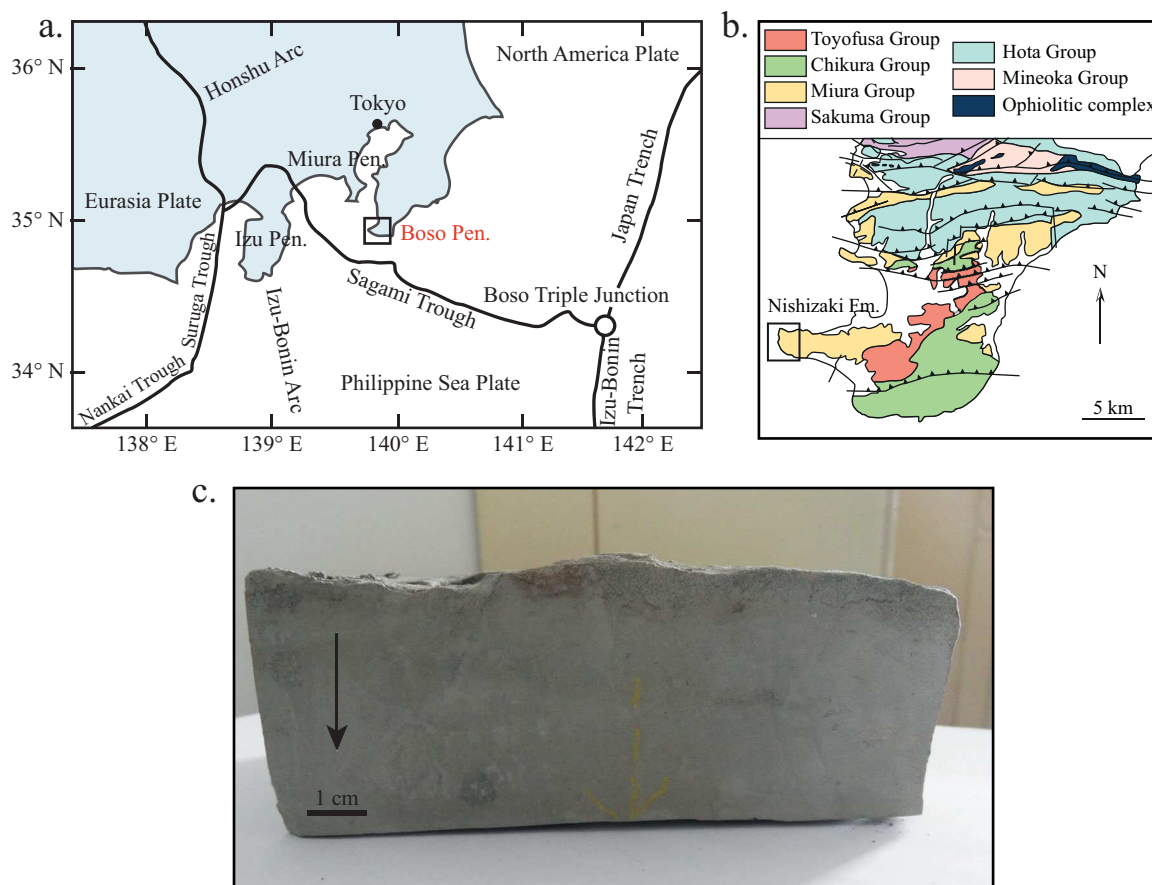


Figure 1. (a) Plate configuration in central Japan and localization of the Miura-Boso peninsula, our sampling site. (b) Zoom on Boso Peninsula and localization of the Nishizaki formation (modified from Yamamoto et al. [2005]). (c) Block of siltstone from Boso peninsula. The arrow is perpendicular to the bedding.

involve both localized structures, such as conspicuous m-scale faults and much more discrete, distributed structures, such as shear band zones, both contributing to the final strain.

The objectives of this paper are twofold: First we want to better analyze the modes of deformation operative in accreted sediments, which are in general submitted to a large magnitude of strain. Second, we want to assess the extent to which such deformation may affect the sediments poroelastic/ V_p properties independently of the sole porosity variations. For this purpose we present a series of triaxial compressive tests conducted on natural siltstones from the Miura-Boso accretionary prism, meant as typical material accreted into the accretionary prism. From these tests we determine the evolution with strain of porosity, axial strain and poroelastic properties. P-wave velocities measurements are done before and after experiments to infer the effect of deformation on P-wave velocity. The distribution and geometry of deformation during each test is reconstructed postmortem from the X-ray microtomographic images of deformed material.

2. Materials and Methods

The experimental deformation and the velocity measurements of water-saturated samples were performed at the Institut des Sciences de la Terre d'Orléans (ISTO). The experimental deformation was performed using a triaxial press (Paterson apparatus). The velocity measurements were performed separately before and after deformation with a dedicated apparatus equipped with acoustic measurement transducers.

2.1. Starting Material

The starting material for experiments is natural clayey siltstones from the Nishizaki formation (Figures 1a and 1b). This formation crops out in the Upper Miocene Miura-Boso accretionary prism, central Japan, which

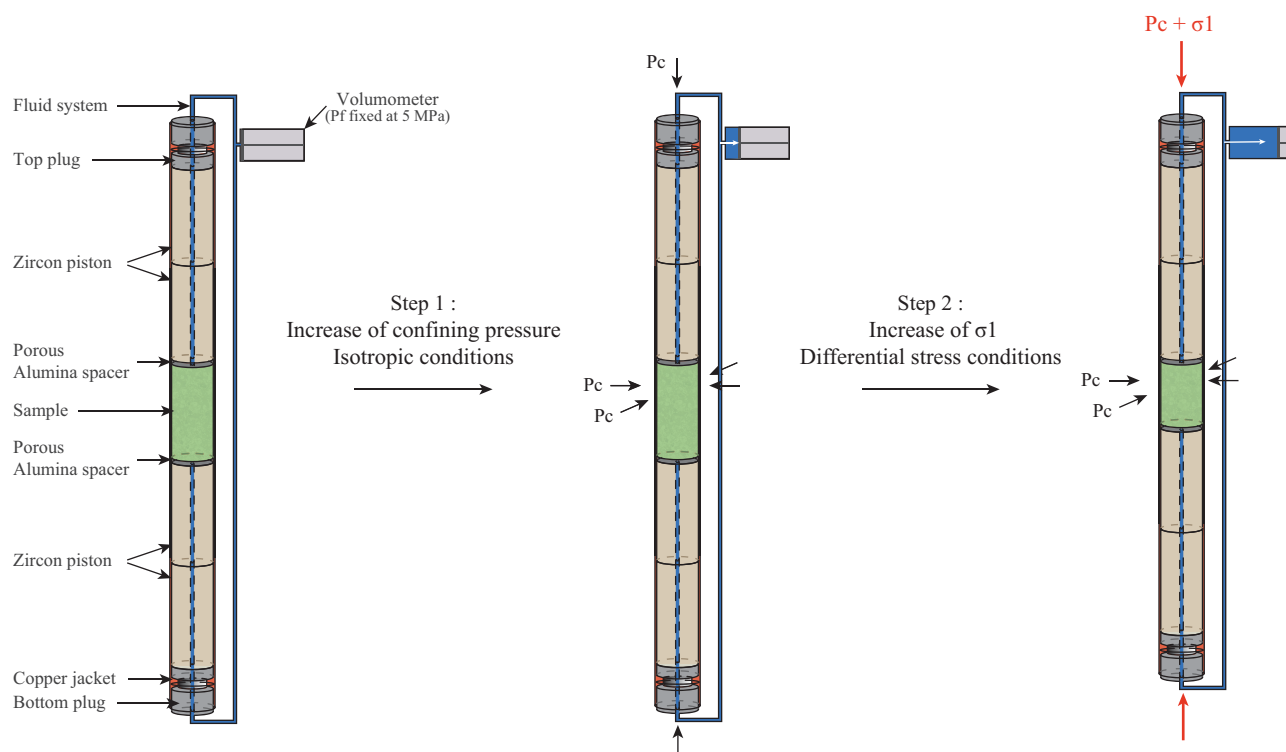


Figure 2. Paterson assembly and principle of experiments.

is a unique on-land example of the shallow parts of accretionary prism. On this site, the maximum burial depth is estimated to have been shallower than 1000 m and maximum paleotemperature ranges between 40 and 52°C [Yamamoto *et al.*, 2005]. As a consequence, diagenesis is not advanced as proved by the abundance of smectite in this area [Kameda *et al.*, 2010]. However, the samples can be partly cemented since the onset of cementation in such sediments could occur at temperature below 55°C [Spinelli *et al.*, 2007]. The deformation is mainly localized on horizontal contraction structures (i.e., duplex structures and imbricate thrusts) between which rocks are almost free from deformation [Yamamoto, 2006]. Thus, samples were carefully selected to avoid large structural features such as faults and did not include scaly fabric (Figure 1c). In summary, the starting material is considered as representative of frontally accreted sediments in a relatively immature state, i.e., before burial and deformation.

X-ray diffraction (XRD) analyses (see supporting information for the detailed procedure) indicate that sediments contain abundant randomly interstratified illite-smectite (I-S) (14 Å peak), as well as illite (10 Å peak), kaolinite + chlorite (7 Å peak), quartz (3.34 Å peak) and plagioclase (3.21–3.18 Å double peak). Mineral composition (estimates from the normalization factors of Underwood *et al.* [2003]) consists of ~ 25 wt.% quartz, ~ 20 wt.% plagioclase, up to 40 wt.% I-S, 10–15 wt.% illite, and 0–5 wt.% kaolinite. The total clay content (I-S + illite + kaolinite (+ chlorite)) reaches 55–60 wt.%. The content of smectite in the I-S layer is estimated to ~ 57 % (± 8 %).

The mean porosity (i.e., pore water volume + smectite interlayer water volume), measured by water immersion, is ~ 43 %. The corrected value, reflecting only the pore water volume gives a porosity of about 34 % (see supporting information for the detailed procedure).

In the following, “natural” or “undeformed sample” refers to the starting material.

2.2. Triaxial Apparatus

Triaxial compressive tests were conducted in a Paterson press [Paterson, 1990] which allows tests in drained conditions (assembly in Figure 2). Prior to experiments, natural samples were saturated by water immersion for several days. Hence, deformation experiments were performed on saturated samples at four different

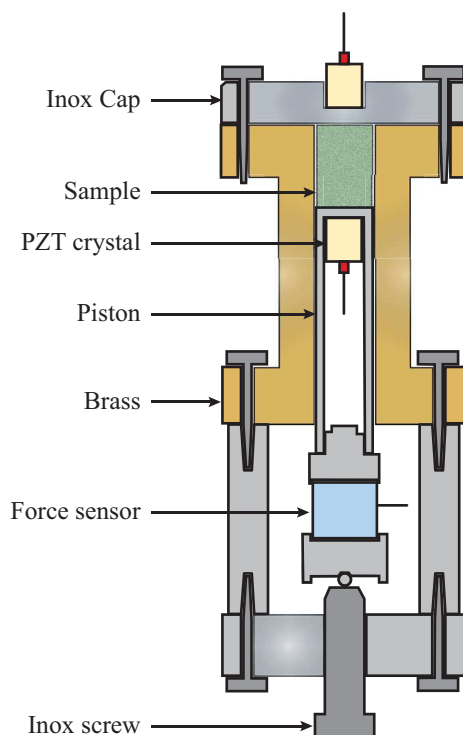


Figure 3. Schematic diagram of the apparatus used for velocity measurements performed in this study.

confining pressures ($P_c = 50, 100, 150$ and 200 MPa) all at room temperature. Here P_c refers to the argon gas pressure that surrounds the sample. This high range of confining pressure was selected to compact the samples in the course of a single experiment (~ 1 day) down to porosities around 10%, i.e., correlatable to material at depths of the order of a few kilometers below seafloor in modern margins.

The cylinder axis of each core was oriented perpendicular to sedimentary bedding and the samples size was ~ 15 mm in diameter and ~ 30 mm in length to keep a length/diameter ratio near 2. In order to see the effect of strain rate ($\dot{\epsilon}$), the experiments have been done at two servo-controlled strain rates ($\dot{\epsilon} = 10^{-5}$ or 10^{-4} s^{-1}). At any time, an internal sensor measures the internal force applied to the sample. From this value of internal force and the section on which it is exerted we derived the stress (σ_1) applied to the sample by using the following equation:

$$\sigma_1 = \frac{F}{S_0}$$

With σ_1 the stress (MPa), F the internal force (N) and S_0 the initial section of the sample (mm^2).

The sample shortening induced by compression is recorded at any time by means of LVDTs (Linear Variable Differential Transformers). This shortening is converted into axial strain (ϵ).

Using capillary tubes connected to an external volumometer, the fluid pressure (P_f) on both flat sides of cylindrical samples was kept constant during all tests at a value of 5 MPa. The fluid expelled from the sample during the experiments was stored in a volumometer (Figure 2), enabling us to calculate the porosity evolution all over the tests.

All tests were carried out according to the same protocol. In the first part of the experiments the confining pressure P_c was increased by step of 10 MPa until 50 MPa and by step of 50 MPa beyond. Steps were separated by intervals of 30 minutes in order to let the sample equilibrate in these new conditions. After reaching the desired P_c , the compression was started at a constant strain rate, with axial force F monitored. In order to evaluate the elastic properties of the samples, this stage was punctuated by several unload-reload cycles conducted at high strain rates, i.e., with an order of magnitude above the monotonic loading rate (i.e., $5.10^{-4} \text{ s}^{-1} \leq \dot{\epsilon} \leq 10^{-3} \text{ s}^{-1}$).

In the following, samples used in triaxial tests will be called “deformed samples.”

2.3. Jacket Correction

Calibration tests were run to evaluate the contribution of the copper jacket on the axial stress measured during triaxial tests (procedure in supporting information). These tests indicate that the contribution of the jacket is of the order of 16% which gives an estimate of the maximum error made in our stress measurements.

2.4. Measurement of P-Wave Velocity

Laboratory measurements of P-wave velocity (V_p) were carried out employing a device equipped with acoustic measurement transducers. This device consists of a hollow cylinder, closed at one end by a fixed cap and at the other end by a mobile piston controlled by a mechanical pressure (screw-nut system) (Figure 3). This is an open system (water is free to escape) in which the sample is placed between the cap and the piston. The stress applied to the sample is controlled by a force sensor placed upstream of the piston.

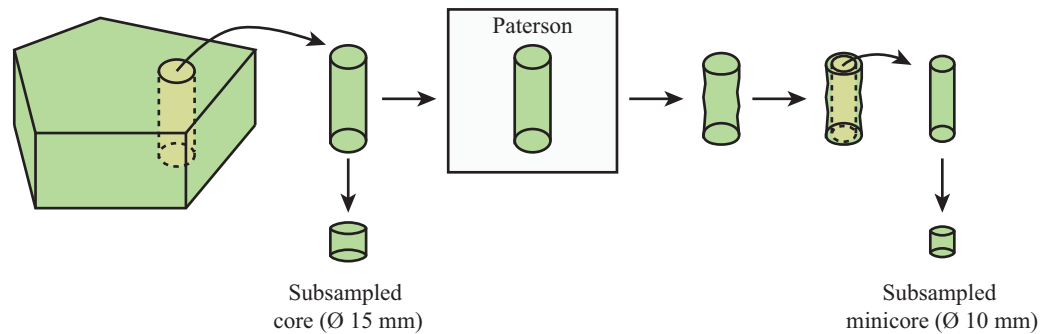


Figure 4. Sampling strategy.

Before starting the tests the device was calibrated with aluminum samples in order to assure the reliability of the results. Then, two series of samples were analyzed. First, we drilled cores from our Boso siltstones samples (starting material). Analyzed samples were ~15 mm in diameter and ~10 mm in length. Second, after unloading, we subsampled Boso siltstones deformed in the Paterson press in order to see the effect of deformation on velocity. The subsampled minicores were ~10 mm in diameter and ~6.5 mm in length (Figure 4). All tests were run on saturated samples at room temperature.

We used a pulse transmission method [Christensen, 1985] to determine P-wave velocities. PZT crystals placed in the piston and in the cap are used as a source-receiver pair for wave propagation experiments. The polarized frequency is fixed at 2 MHz. Measurements of velocity were done up to 400 daN (i.e., ~22.6 MPa). Waveforms were recorded at each step of stress increase for a period of 30 s. The waveforms are then averaged in order to minimize the background noise and then determine more precisely the travel time. The accuracy in the determination of travel time is $\pm 0.2 \mu\text{s}$. Then for a core sample 9.6 mm long and a velocity of 2140 m s^{-1} , precision is estimated to be $\sim \pm 95 \text{ m s}^{-1}$.

2.5. Computed Tomography Scans Analysis

Microtomography analyses were performed using an industrial computed tomography (CT) device Nanotom 180NF (GE Phoenix|x-ray, Wunstorf, Germany) available at the ISTO. This unit has a 180 kV nanofocus X-ray tube and a digital detector array (2304×1152 pixels Hamamatsu detector).

The voxel resolution ranges between 26 and 36 μm depending on the initial sample size.

3. Results

3.1. Triaxial Tests

A summary of the experimental conditions for each test is presented in table 1.

3.1.1. Porosity Evolution

In the following, the values of porosity presented are calculated from the initial corrected value of porosity (i.e., initial pore volume) and assuming that the volume expelled during deformation is only due to pore space squeezing.

Table 1. Summary of Characteristics of Triaxial Tests

Experiment Number	Sample	Initial Conditions			Experimental Conditions and Results					
		Length (mm)	Diameter (mm)	Mean Corrected Porosity (%)	Mean P-Wave Velocity (m/s)	Confining Pressure (MPa)	Strain Rates Applied (s^{-1})	Axial Strain Reached (%)	Porosity After Isotropic Loading (%)	Porosity After Complete Triaxial Test (%)
PP 319	Siltstone	33.60	14.79	34 ± 2	2132 ± 99	50	$10^{-5}, 10^{-4}, 5.10^{-4}$	40.95	24.7	12.3
PP 314	Siltstone	36.18	14.79	34 ± 2	2132 ± 99	100	$10^{-5}, 10^{-3}$	24.00	21.7	14.9
PP 334	Siltstone	34.10	14.84	34 ± 2	2132 ± 99	150	$10^{-5}, 10^{-4}, 5.10^{-4}$	34.60	14.4	8.3
PP 335	Siltstone	35.37	14.82	34 ± 2	2132 ± 99	150	$10^{-5}, 10^{-4}, 5.10^{-4}$	34.25	12.1	4.4
PP 322	Siltstone	26.47	14.75	34 ± 2	2132 ± 99	200	$10^{-5}, 10^{-4}, 5.10^{-4}$	39.07	8.8	3.7

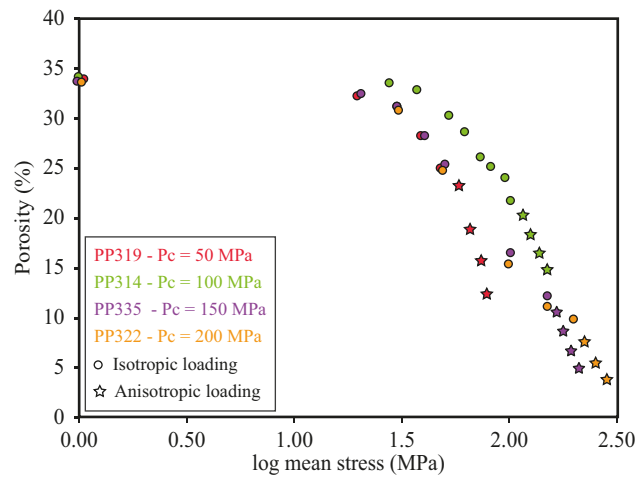


Figure 5. Evolution of porosity with mean stress under anisotropic and isotropic stress conditions. Values of porosity are calculated from the volume of water expelled during experiments recorded by the volumometer. Porosities at beginning are measured by water immersion and corrected from the smectite water volume.

is not linear and the slope $d\sigma/d\varepsilon$ decreases with strain, either regularly (PP 314, PP 319) or not (PP 334, PP 335, PP 322). Moreover, an increase in strain rate results in a slight, but systematic increase in deviatoric stress (velocity-strengthening behavior).

At the end of experiments axial strain reached nearly 40 % (value limited by technical constraints). Despite this strong deformation, no drastic stress drop, characteristic of rupture of the sample, occurred during the course of any experiment.

3.1.3. Microstructures of Deformation

Macroscopic observations of the samples at the end of experiments show that deformation proceeds from a large (width ~ 14 mm) shear band, sometimes crosscut by a net fault plane, both being responsible for the misalignment of the samples ends (Figure 6c). CT-scan analysis shows first that the fault plane is characterized by a higher porosity than surrounding matrix (Figure 7a). Quantitative estimates of the displacement on the fault indicate that it accommodates only a small fraction of overall shear ($<5\%$), the rest being accommodated by the large shear zone (see supporting information). The material within the shear zone has the same porosity as the surrounding volume indicating that it has been affected by porosity decrease while it was accommodating strain. As this process combines porosity reduction and shearing, we called it “compaction-assisted shearing.”

The chronology between shearing and faulting was determined from a few observations. First, while experiments PP 334 and PP 322 show the presence of both shear zone and fault, only shearing occurred and no rupture plane was initiated in PP 314 and PP 319. Therefore, faulting is posterior to compaction-assisted shearing. Moreover at the end of experiment, the fault appears as a net and rectilinear plane, which implies that shear zone was inactive during faulting (otherwise the fault plane would be deformed/curved). As a result, we propose that faulting took over compaction-assisted shearing in the final part of the experiments. On the basis of this hypothesis and the calculations detailed in the supporting information, the respective timing of shearing and faulting is labeled in Figure 6 for each experiment.

3.1.4. Elastic Deformation

Young’s modulus (E) is rather constant in the range from 100 to 200 MPa of confining pressure (equivalent to $14.6 < \text{porosity} < 4.2$ %) (Figure 8a). However, E decreases with increasing axial strain independently of the confining pressure value (Figure 8b). The decrease is marked by a drastic drop of the modulus for an axial strain between 15 and 25%.

3.2. Velocity Tests

In all samples where velocity measurements were carried out (undeformed/natural and deformed ones), P-wave velocities increase linearly with the increase in effective pressure (Figure 9). However, the comparison

Porosity loss occurs during the whole tests (Figures 5 and 6). Curves “porosity versus log (mean stress)” (with mean stress = $\frac{\sigma_1 + 3P_c}{3}$) are typical consolidation curves with a systematic slope break around 30 MPa (Figure 5). Beyond this yield stress, the slopes for each tests are rather constant whatever the loading geometry (isotropic versus anisotropic) involving that porosity is at first order controlled by the mean stress.

3.1.2. Macroscopic Mechanical Behavior

All the samples deformed in compression show the same trend irrespective of the confining pressure value (Figure 6). Throughout the experiments the differential stress increases with axial strain. The strain hardening behavior

is not linear and the slope $d\sigma/d\varepsilon$ decreases with strain, either regularly (PP 314, PP 319) or not (PP 334, PP 335, PP 322). Moreover, an increase in strain rate results in a slight, but systematic increase in deviatoric stress (velocity-strengthening behavior).

At the end of experiments axial strain reached nearly 40 % (value limited by technical constraints). Despite this strong deformation, no drastic stress drop, characteristic of rupture of the sample, occurred during the course of any experiment.

Macroscopic observations of the samples at the end of experiments show that deformation proceeds from a large (width ~ 14 mm) shear band, sometimes crosscut by a net fault plane, both being responsible for the misalignment of the samples ends (Figure 6c). CT-scan analysis shows first that the fault plane is characterized by a higher porosity than surrounding matrix (Figure 7a). Quantitative estimates of the displacement on the fault indicate that it accommodates only a small fraction of overall shear ($<5\%$), the rest being accommodated by the large shear zone (see supporting information). The material within the shear zone has the same porosity as the surrounding volume indicating that it has been affected by porosity decrease while it was accommodating strain. As this process combines porosity reduction and shearing, we called it “compaction-assisted shearing.”

The chronology between shearing and faulting was determined from a few observations. First, while experiments PP 334 and PP 322 show the presence of both shear zone and fault, only shearing occurred and no rupture plane was initiated in PP 314 and PP 319. Therefore, faulting is posterior to compaction-assisted shearing. Moreover at the end of experiment, the fault appears as a net and rectilinear plane, which implies that shear zone was inactive during faulting (otherwise the fault plane would be deformed/curved). As a result, we propose that faulting took over compaction-assisted shearing in the final part of the experiments. On the basis of this hypothesis and the calculations detailed in the supporting information, the respective timing of shearing and faulting is labeled in Figure 6 for each experiment.

Young’s modulus (E) is rather constant in the range from 100 to 200 MPa of confining pressure (equivalent to $14.6 < \text{porosity} < 4.2$ %) (Figure 8a). However, E decreases with increasing axial strain independently of the confining pressure value (Figure 8b). The decrease is marked by a drastic drop of the modulus for an axial strain between 15 and 25%.

In all samples where velocity measurements were carried out (undeformed/natural and deformed ones), P-wave velocities increase linearly with the increase in effective pressure (Figure 9). However, the comparison

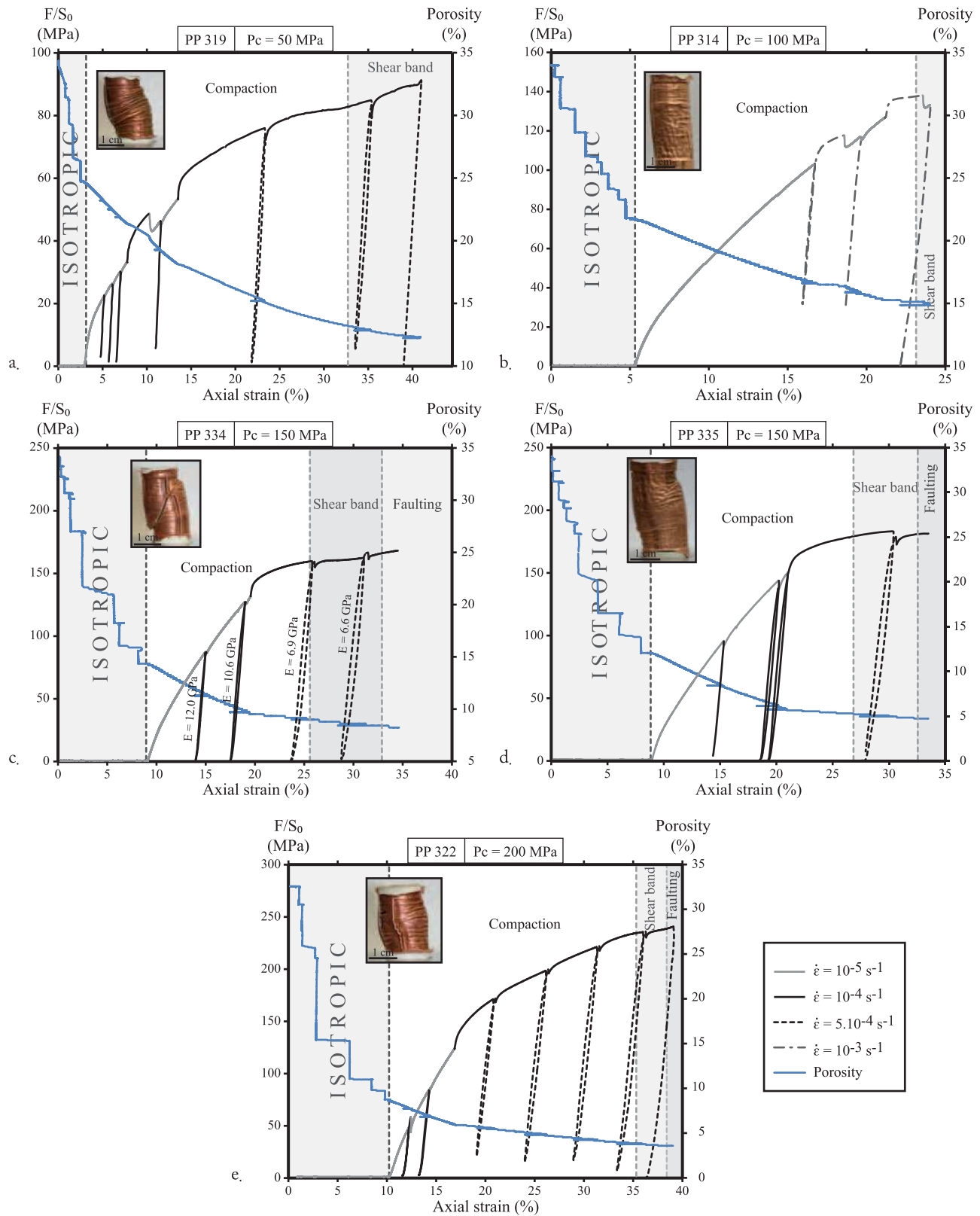


Figure 6. Compilation of five triaxial tests showing the evolution of differential stress (F/S_0) and porosity with the axial strain for different values of confining pressure at (a) 50 MPa, (b) 100 MPa, (c and d) 150 MPa, and (e) 200 MPa. Pictures taken at the end of each tests are shown. Transition of one mode of deformation to another (labeled for each test) is calculated from the CT scans realized postmortem (see text for details).

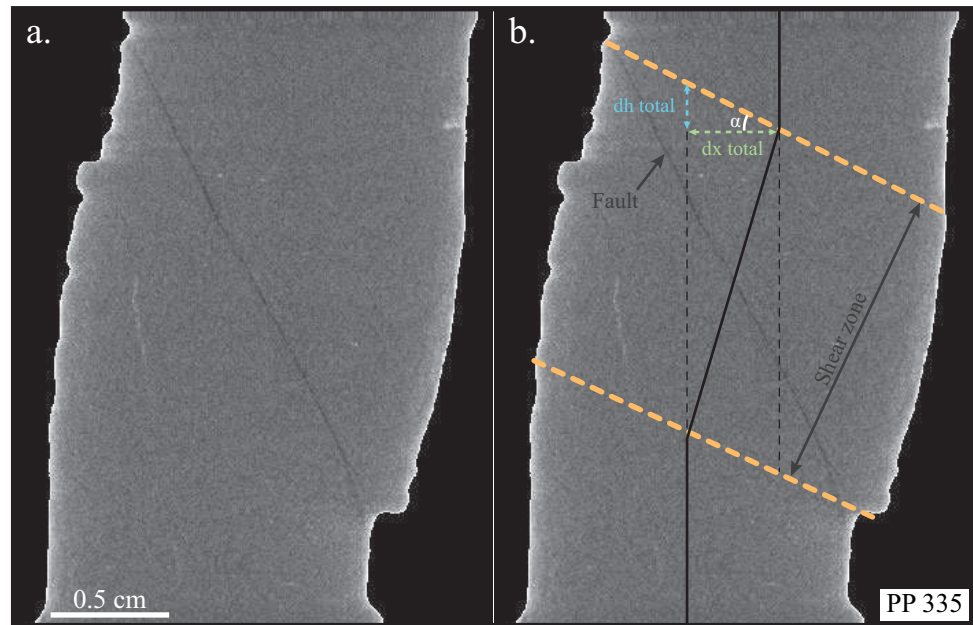


Figure 7. (a) Representative CT scan analysis obtained after PP 335 triaxial test. The central part of the sample was affected by diffuse shearing, resulting in the misalignment of upper and lower ends of the sample and the smooth bending of its vertical surfaces. This shear band is crosscut by a thin fault with a lower density (the thin, diagonal, black line), which in the end of the experiment took over the deformation and set off the two halves of the sample. (b) Sketch of the misalignment and method to calculate the shift induced by deformation. “dx total” and “dh total” refer to the horizontal and vertical shift, respectively, induced by the combination of shearing and faulting.

between the V_p measured in the natural sample and the experimentally deformed ones, reveals that deformation induced two major effects:

- (1) Deformation decreases V_p . Indeed, in spite of their much lower porosity (down to 8%), deformed samples have a velocity comparable to the undeformed sample with its large porosity (34%), for effective pressure (P_{eff}) up to 12 MPa.
- (2) Deformation increases the sensitivity to effective pressure $\frac{\partial V_p}{\partial P_{eff}}$. Deformed samples exhibit $\frac{\partial V_p}{\partial P_{eff}}$ about two times larger than the natural sample.

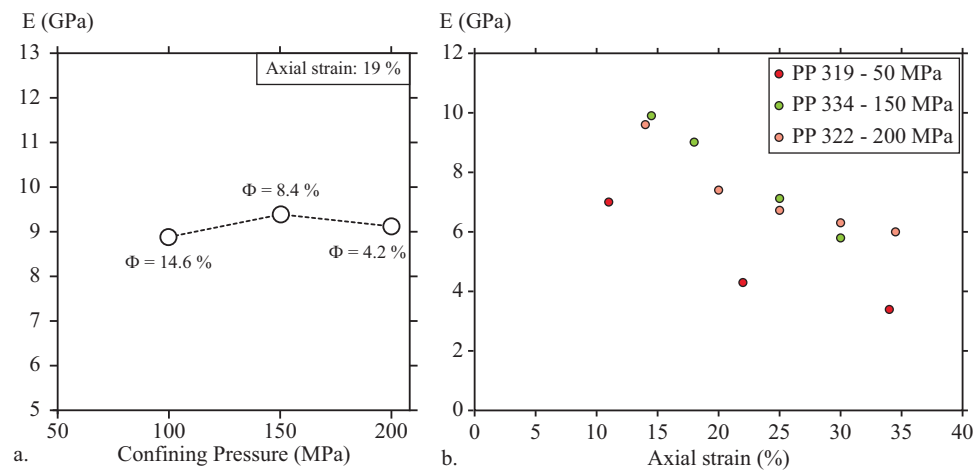


Figure 8. Graphs showing the evolution of elastic properties with stress and strain. (a) Evolution of Young’s modulus with P_c/Φ for a fixed axial strain of 19%. (b) Evolution of Young’s modulus with axial strain for different values of P_c (50, 150, and 200 MPa).

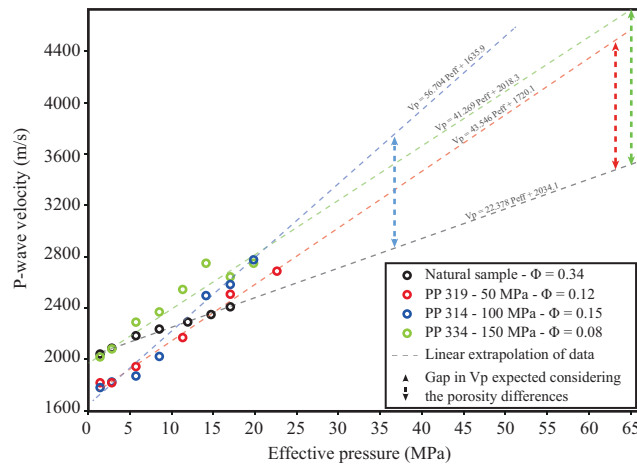


Figure 9. P-wave velocities measured in this study for natural sample and after each triaxial test (the maximum error is +120, -140 m s⁻¹ and does not appear for clarity reasons) and linear extrapolation of data.

4. Discussion

4.1. Modes of Deformation: Localized Fault Versus Wide Shear Band

At the end of our experiments, the compacting shear zone is crosscut by a failure plane. This transition between distributed and localized deformation takes place at high strain, high stress and low porosity, which renders difficult to pinpoint the parameter responsible for localizing deformation.

In order to discriminate between these different parameters, we made a review of natural structures (normal faults, thrusts, deformation bands) found in cores from

different locations of the Nankai subduction zone (incoming sediments, toe of the prism, splay fault and imbricated thrust sheet) (Figure 10). All along the subduction zone, deformation bands and faults are systematically associated. In terms of spatial distribution faults and deformation bands are found all over the range of depth explored in IODP cores (from 0 (sites C0011 and C0012) to 1100 m below the seafloor (site C0002)) either in distributed zones (e.g., sites C0012, C0001) or in restricted, concentrated zones (e.g., sites C0002, C0007) (C0001, C0007: *Kinoshita et al. [2009a], [Kinoshita et al., 2009e]*; C0002: *Kinoshita et al. [2009b], Kopf et al. [2011]*; C0011: *Saffer et al. [2010], Saito et al. [2010a], Henry et al. [2012a]*; C0012: *Saito et al. [2010b], Henry et al. [2012b]*). Cross-cutting relationships between these structures are not

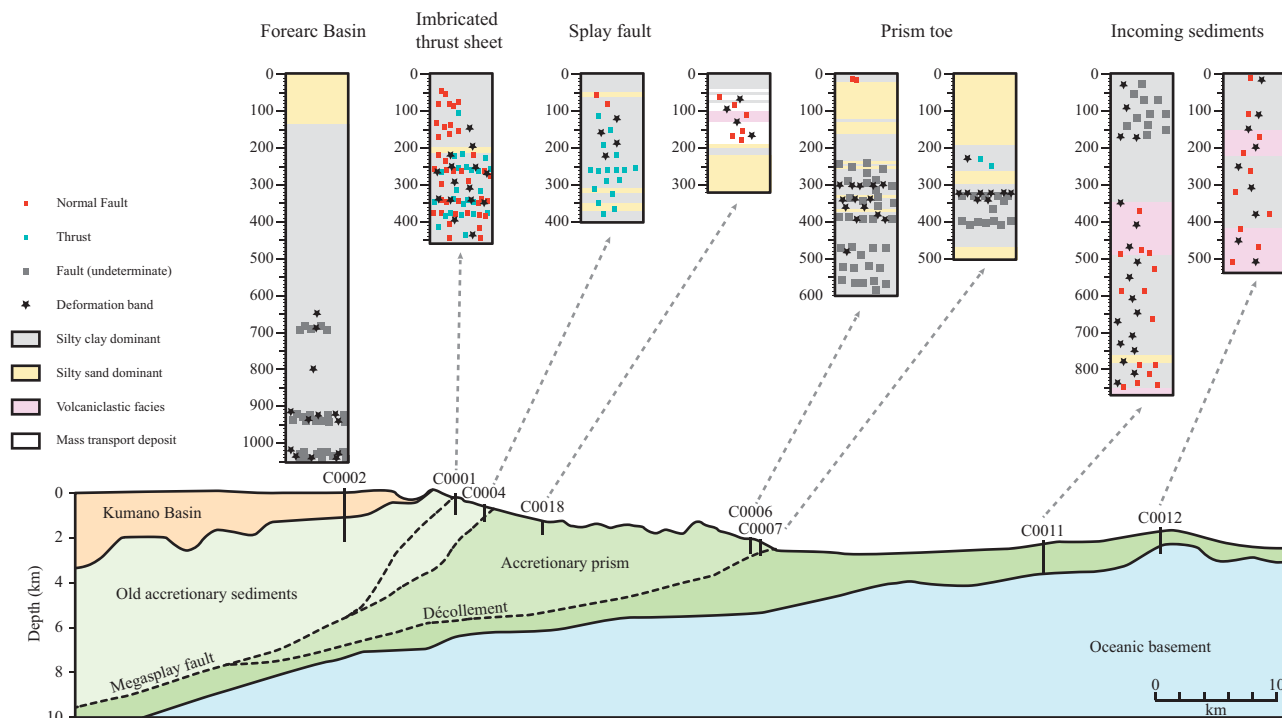


Figure 10. Compilation of structural data (deformation bands, thrusts and normal faults) from NanTroSEIZE project. References are as follows: C0001: *Kinoshita et al. [2009a]*; C0002: *Kinoshita et al. [2009b], Kopf et al. [2011]*; C0004: *Kinoshita et al. [2009c]*; C0006: *Kinoshita et al. [2009d]*; C0007: *Kinoshita et al. [2009e]*; C0011: *Saffer et al. [2010], Saito et al. [2010a]*; C0012: *Saito et al. [2010a], Henry et al. [2012b]*; C0018: *Henry et al. [2012c]*.

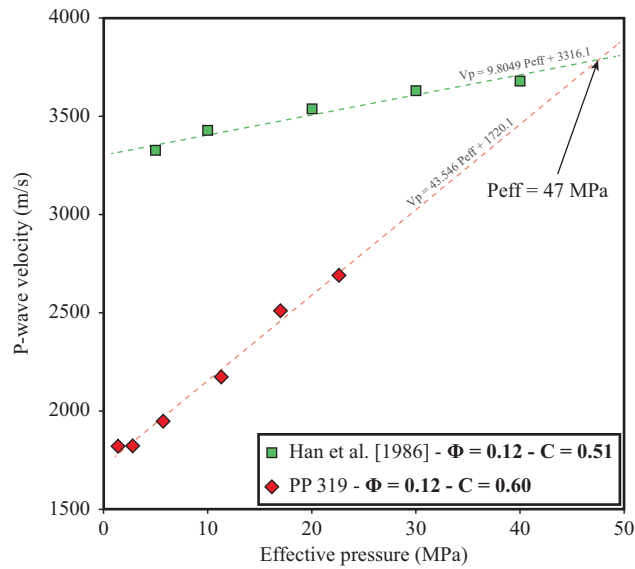


Figure 11. P-wave velocity versus effective pressure. Comparison of our results and experimental results of Han et al. [1986] for samples with same porosity (0.12) and similar clay content (0.5–0.6).

systematic, as can be seen in the site C0001 where deformation bands as well as normal, thrust and strike-slip faults are superimposed on each other [Kinoshita et al., 2009a].

In the case of a control of the porosity on the deformation mode (fault versus band), one would expect to see deformation bands homogeneously distributed with depth (i.e., formed at shallow depth/high porosity then buried at various depths) and systematically crosscut by faults (formed at larger depth/lower porosity). None of such criteria of spatial distribution or crosscutting relationship is fulfilled, leading us to propose that the alternation between deformation bands and faults is inde-

pendent of the porosity and is rather the result of variations in stress/strain rate over the seismic cycle.

4.2. Effect of Macroscopic Deformation on Poroelastic Properties

4.2.1. Observed Variations in Physical Properties

During the mechanical experiments described here, there are strong variations in the poroelastic properties of the sample material, which are apparent through the following variations:

- (1) A decrease in Young's modulus, observed during the successive unload-reload cycles carried out in the course of experiments (Figure 8b).
- (2) A decrease in V_p for post experiments measurements, carried out in the low effective pressure range: V_p measured at $P_{eff} \leq 12$ MPa in the high porosity (34%) natural sample (i.e., the starting material before triaxial test) is similar or higher than the V_p measured postmortem in the deformed materials (i.e., the same material but deformed in triaxial press), which have been affected by a large porosity drop (final porosities < 15%) (Figure 9).
- (3) An increase in sensitivity of V_p to P_{eff} (Figures 9 and 11). For similar porosity and clay content (C), in the deformed sample PP 319 ($\Phi = 0.12$; $C = 0.60$), $\frac{\partial V_p}{\partial P_{eff}}$ is equal to $43 \text{ m s}^{-1}/\text{MPa}$ (Figure 11), while in a similar ($\Phi = 0.12$; $C = 0.51$), natural sample used by Han et al. [1986], $\frac{\partial V_p}{\partial P_{eff}}$ is equal to $9.8 \text{ m s}^{-1}/\text{MPa}$, i.e., four times smaller. Furthermore, for the siltstones used here, $\frac{\partial V_p}{\partial P_{eff}}$ is between two and three times larger in deformed samples (PP314, 319 and 334) than in original, undeformed material (Figure 9 and Table 2).

4.2.2. Microscopic Process at Stake: Cement Breakage and Increase in Crack Density

The microstructural evolution responsible for the decrease in stiffness cannot be unambiguously determined, but several factors point to an increase in crack density during triaxial deformation experiments, resulting for example from the destruction of intergrain cement. First, the decrease in stiffness along with porosity decrease/stress increase (= compaction) (Figure 8b) is completely opposite to consolidation experiments on powders, showing on the contrary an increase in stiffness with compaction [Karig and Hou, 1992]. Therefore, in experimentally deformed samples, the destruction of a preexisting, stiffening structure such as cement, counterbalances and has even a larger influence than the stiffening effect of porosity decrease/stress increase. Second, the increase in sensitivity of V_p to P_{eff} can also be interpreted as a result of increased crack density in experimentally deformed samples, as suggested in Raimbourg et al. [2011] in shallow

Table 2. Conditions and Results of P-Wave Measurements

Type of Sample	Sample	Porosity (%)	Axial Strain (%)	Range of Effective Pressure for P-Wave Measurements (MPa)	P-Wave Linear Regression	95% Confidence Interval on the Slope
Starting material	GJ02	34 ± 2	0.00	1.4–17	$V_p = 22.378 P_{eff} + 2034.1$	± 2.5
Deformed in triaxial press	PP 319	12.3	40.95	1.4–22.6	$V_p = 43.536 P_{eff} + 1720.1$	± 5.6
	PP 314	14.9	24.00	1.4–19.8	$V_p = 56.704 P_{eff} + 1635.9$	± 10.6
	PP 334	8.3	34.60	1.4–19.8	$V_p = 41.269 P_{eff} + 2018.3$	± 12.3

sediments. *Ougier-Simonin et al.* [2011] have also shown the strong dependence of V_p to effective pressure ($\frac{\partial V_p}{\partial P_{eff}} = 40 \text{ m s}^{-1}/\text{MPa}$) in thermally cracked glass, with values similar to the ones reported here for deformed samples (table 2).

4.2.3. Range of Efficiency of Cement Breakage With Increasing P_{eff}

Comparing undeformed and deformed samples with the same porosity (Figure 11), there is an effective pressure beyond which V_p of deformed samples reach the one of undeformed samples, i.e., the effect of deformation vanishes. When comparing the undeformed and deformed samples of the same material (Boso siltstones), the precise determination of this effective pressure implies to take also into account the variable porosities between the different samples. In other words, the question is at which effective pressure the velocity difference between deformed samples (Φ from 8 to 15%) and undeformed one ($\Phi = 34\%$) could be attributed solely to the porosity difference and not to the peculiar high density of microcracks in the deformed samples?

In order to answer it we have first to infer the respective dependence of V_p to effective pressure and porosity. V_p - Φ relationships available, determined principally in basinal settings, show indeed an increase of V_p with decreased Φ , but this effect incorporates implicitly a correlated increase in depth/ P_{eff} with the decrease in Φ [e.g., *Erickson and Jarrard*, 1998]. To deconvolute porosity and P_{eff} dependence of V_p , one can use the experimental data of *Han et al.* [1986] (Figure 11), yielding an increase in V_p of 9.8 m s^{-1} , for an increase of 1 MPa of effective pressure, for a roughly constant porosity. Using this value, one can compare then the V_p of samples with 30 % (2206 m s^{-1}) and 10 % porosity (3708 m s^{-1}) in the V_p - Φ relationships from *Eberhart-Phillips et al.* [1989] (Figure 12). In this graph, all the V_p data correspond to conditions of in situ effective pressure under hydrostatic gradient and the maximal difference in effective pressure between the samples with 10% and 30% porosity is $\sim 58 \text{ MPa}$ [*Jssler*, 1992]. The contribution of effective pressure to the increase in V_p is then 568 m s^{-1} , so that, by difference, the contribution of porosity decrease is 934 m s^{-1} (i.e., V_p increases by $\sim 47 \text{ m s}^{-1}$ for each percent of porosity loss).

Applying these results to figure 9, the difference in V_p expected between PP 314 ($\Phi = 15\%$) and the natural sample GJ02 ($\Phi = 34\%$), if V_p depended only on porosity, would be 893 m s^{-1} , a difference reached for an effective pressure of $\sim 37 \text{ MPa}$. A similar range of effective pressure can be deduced from Figure 11. Indeed, for material with similar porosity and clay content, the experimentally deformed material has lower V_p than natural one for $P_{eff} \leq 47 \text{ MPa}$. This range of P_{eff} is in good agreement with other studies that have shown that cracks remain open, hence lower P-wave velocities, until a confining pressure of about

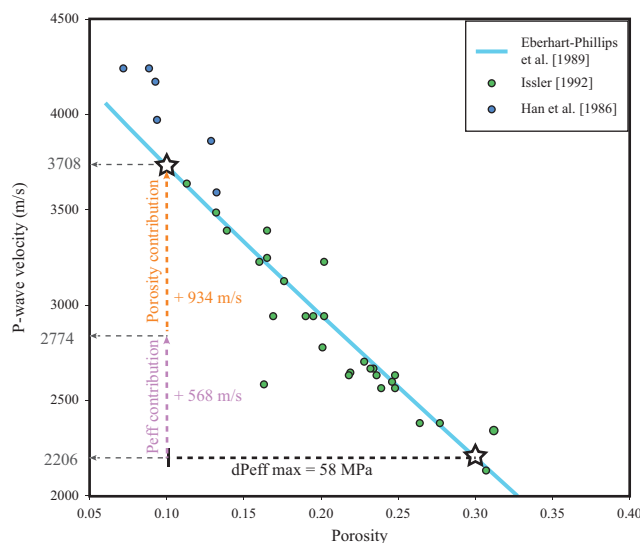


Figure 12. Compilation of porosity-velocity experimental [*Han et al.*, 1986; *Eberhart-Phillips et al.*, 1989] and log-based relationships [*Jssler*, 1992], and calculation of the respective contribution of effective pressure increase and porosity decrease on the difference in V_p of two samples (porosity = 30 and 10%).

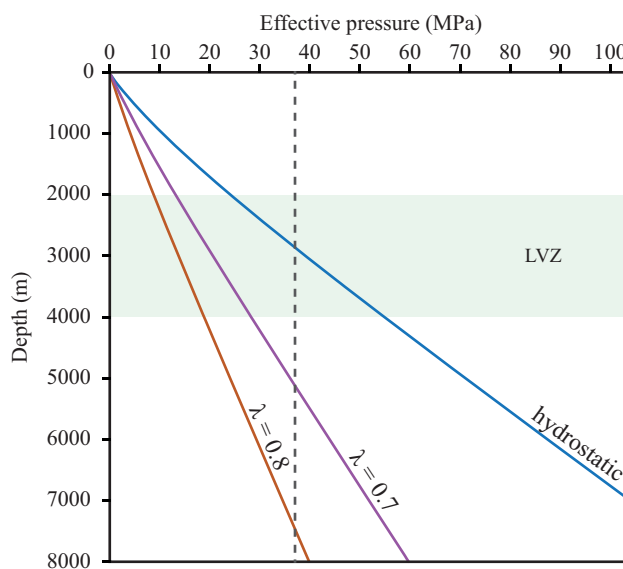


Figure 13. Effective pressure gradients for different values of fluid ratio. The dashed line represents the effective pressure until which deformation (microcracks) has an influence on V_p inducing negative anomalies of V_p . The extent of the low velocity zone (LVZ) is as described by *Kitajima and Saffer* [2012] for the Nankai accretionary prism.

40 MPa [Ougier-Simonin *et al.*, 2011; Guéguen *et al.*, 2011; Fortin *et al.*, 2011].

In conclusion, we propose that for effective pressure below 40 MPa, anomalously high density of microcracks resulting from cement destruction during deformation could induce low values of V_p . At larger P_{eff} , cracks close and the effect of deformation on V_p is no longer significant.

4.3. V_p Anomalies in Accretionary Prisms: Evidences for Fluid Overpressure?

Seismic reflection methods are widely used to image large-scale and deep structures within accretionary prisms. For the Nankai Trough subduction zone, sev-

eral studies have shown that the underthrust section, below the plate boundary, is characterized by low seismic impedance [Bangs and Shipley, 1999; Park *et al.*, 2002; Bangs *et al.*, 2009]. As well, a recent study made by *Kitajima and Saffer* [2012] revealed two broad regions of low seismic velocity with respect to the surrounding material at the same depth, along the Nankai subduction plate boundary megathrust offshore SW Japan. The upper one, at depth between 2 and 4 km below the seafloor, is located above the active décollement, within the accretionary prism. Low seismic velocity/impedance is commonly interpreted as reflecting high porosity of sediments with respect to the surrounding sediments [Erickson and Jarrard, 1998; Hoffman and Tobin, 2004]. The results discussed in the section above lead us to evaluate the possible implication of another factor for these low velocity anomalies: cement breakage inducing microcracks. Indeed, unlike sedimentary basins without tectonics, where sedimentary rocks are continuously cemented during diagenesis, the active deformation in accretionary prism may lead locally and transiently to the destruction of the cement and to a decrease in V_p [Raimbourg *et al.*, 2011]. As discussed above, the conditions where cracks are open and V_p decreased depend on effective pressure (i.e., $P_{eff} < 40$ MPa), hence the depth range where this phenomenon is active is dependent of the fluid pressure gradient.

In Figure 13 are reported different effective pressure trends in function of fluid pressure ratio λ ($= P_{fluid}/P_{bulk}$). In accretionary margins the burial is tectonically controlled and the fluid pressure is probably close to lithostatic (e.g., *Moreno et al.* [2014] estimated a mean value of λ ($= P_{fluid}/P_{bulk}$) of 0.98 for the Chilean margin). In Nankai accretionary prism, which is characterized by a low taper angle and a large proportion of clay, the pore fluid ratio (λ) is about 0.7–0.8 near the décollement [Saffer, 2003]. In these conditions of high fluid pressure, the zone between 2 and 4 km depth, where *Kitajima and Saffer* [2012] document a large low velocity zone, would be submitted to effective pressure between 9 and 29 MPa, i.e., well below 40 MPa. The low V_p zone corresponds to underplated material that is probably affected by high strain inducing cement breakage and hence cracks opening. Therefore, the velocity anomaly detected in Nankai accretionary prism between 2 and 4 km depth could be for part the consequence of the intense deformation of the material within it. In conclusion, in the shallow ($P_{eff} < 40$ MPa, $z < 8$ km assuming $\lambda = 0.8$) domains of accretionary prism, anomalies in velocity, which are often interpreted as reflecting solely fluid overpressure within underthrust sediments could also be the consequence of crack formation resulting from intergrain cement breakage during deformation.

5. Conclusion and Perspectives

In this experimental study we conducted five triaxial compressive tests to assess the deformation style and the evolution of mechanical properties (rheology, elastic modulus, P-wave velocity) of sedimentary rocks analogous to sediments entering subduction zones.

Results of experiments show that deformation proceeds by two modes, both associated with strain/velocity hardening: compaction assisted shearing and faulting characterized by dilatancy. The combination of our experimental data with a detailed review of IODP cores observations has also shown that the mode of deformation within the accretionary prism (localized versus distributed) is controlled by the variations in stress/strain rate over the seismic cycle and is independent of the porosity.

Finally, we show that cement breakage that occur during deformation has drastic effect on physical properties of rocks including (1) a decrease in Young's modulus (2) a decrease in V_p and, (3) an increase in sensitivity of V_p to P_{eff} . Such effects induce negative anomalies of V_p that are persistent for effective pressure up to 40 MPa. As a result, the anomaly in V_p observed at 2–4 km depth in Nankai accretionary prism and interpreted as underplated package could reflect, in an environment of elevated pore pressure (typical of accretionary prism), sediment deformation (i.e., cracks formation during cement breakage) rather than anomalously high porosity/pore pressure.

Acknowledgments

Data supporting Figure 10 are available from the IODP expedition reports database (expeditions: 314, 315, 316, 319, 322, 332, and 333). This work has received funding from the program SYSTER (CNRS-INSU) and the European Research Council (ERC) under the seventh Framework Programme of the European Union (ERC Advanced Grant, grant agreement No 290864, RHEOLITH). We thank two anonymous reviewers for their relevant and constructive comments that significantly improved this paper.

References

- Bangs, L. B., and T. H. Shipley (1999), Fluid accumulation and channeling along the northern Barbados Ridge decollement thrust, *J. Geophys. Res.*, 104(B9), 20,399–20,414.
- Bangs, N. L. B., G. F. Moore, S. P. S. Gulick, E. M. Pangborn, H. J. Tobin, S. Kuramoto, and A. Taira (2009), Broad, weak regions of the Nankai Megathrust and implications for shallow coseismic slip, *Earth Planet. Sci. Lett.*, 284(1–2), 44–49, doi:10.1016/j.epsl.2009.04.026.
- Bray, C. J., and D. E. Karig (1985), Porosity of sediments in accretionary prisms and some implications for dewatering processes, *J. Geophys. Res.*, 90(B1), 768–778, doi:10.1029/JB090iB01p00768.
- Byrne, T., and D. Fisher (1990), Evidence for a weak and overpressured décollement beneath sediment-dominated accretionary prisms, *J. Geophys. Res.*, 95(B6), 9081–9097, doi:10.1029/JB095iB06p09081.
- Christensen, N. I. (1985), Measurements of dynamic properties of rock at elevated temperatures and pressures, in *Measurement of Rock Properties at Elevated Pressures and Temperatures*, vol. 869, edited by H. J. Pincus and E. R. Hoskins, American Society for Testing and Materials, Philadelphia, pp. 93–107.
- Eberhart-Phillips, D., D. Han, and M. D. Zoback (1989), Empirical relationships among seismic velocity, effective pressure, porosity, and clay content in sandstone, *Geophysics*, 54(1), 82–89.
- Erickson, S. N., and R. D. Jarrard (1998), Velocity-porosity relationships for water-saturated siliciclastic sediments, *J. Geophys. Res.*, 103(B12), 30,385–30,406.
- Fortin, J., S. Stanchits, S. Vinciguerra, and Y. Guéguen (2011), Influence of thermal and mechanical cracks on permeability and elastic wave velocities in a basalt from Mt. Etna volcano subjected to elevated pressure, *Tectonophysics*, 503(1–2), 60–74, doi:10.1016/j.tecto.2010.09.028.
- Guéguen, Y., M. Adelinet, A. Ougier-Simonin, J. Fortin, and A. Schubnel (2011), How cracks modify permeability and introduce velocity dispersion: Examples of glass and basalt, *Leading Edge*, 30(12), 1392–1398.
- Han, D., A. Nur, and D. Morgani (1986), Effects of porosity and clay content on wave velocities in sandstones, *Geophysics*, 51(11), 2093–2107.
- Henry, P., T. Kanamatsu, K. Moe, and Expedition 333 Scientists (2012a), *Proceedings of the Integrated Ocean Drilling Program*, 333, Site C0011, Ocean Drill. Program, College Station, Tex.
- Henry, P., T. Kanamatsu, K. Moe, and Expedition 333 Scientists (2012b), *Proceedings of the Integrated Ocean Drilling Program*, 333, Site C0012, Ocean Drill. Program, College Station, Tex.
- Henry, P., T. Kanamatsu, K. Moe, and Expedition 333 Scientists (2012c), *Proceedings of the Integrated Ocean Drilling Program*, 333, Site C0018, Ocean Drill. Program, College Station, Tex.
- Hoffman, N. W., and H. J. Tobin (2004), 11. An empirical relationship between velocity and porosity for underthrust sediments in the Nankai Trough accretionary prism, in *Proceedings of the Integrated Ocean Drilling Program*, 190/196, edited by H. Mikada et al., Ocean Drill. Program, College Station, Tex., pp. 1–23.
- Hunze, S., and T. Wonik (2007), Compaction in the Nankai and Barbados accretionary prisms: New insights from logging-while-drilling data: Accretionary prisms, *Geochem. Geophys. Geosyst.*, 8, Q02003, doi:10.1029/2006GC001277.
- Issler, D. R. (1992), A new approach to shale compaction and stratigraphic restoration, Beaufort-Mackenzie Basin and Mackenzie Corridor, Northern Canada (1), *AAPG Bull.*, 76(8), 1170–1189.
- Kameda, J., Y. Yamamoto, and G. Kimura (2010), Smectite swelling in the Miura-Boso accretionary prism: Possible cause for incipient décollement zone formation, *Tectonophysics*, 494(1–2), 75–84, doi:10.1016/j.tecto.2010.08.008.
- Karig, D. E. (1996), 20. Uniaxial reconsolidation tests on porous sediments: Mudstones from site 897, in *Proceedings of the Integrated Ocean Drilling Program*, 149, edited by R. B. Whitmarsh et al., Ocean Drill. Program, College Station, Tex., pp. 363–373.
- Karig, D. E., and G. Hou (1992), High-stress consolidation experiments and their geologic implications, *J. Geophys. Res.*, 97(B1), 289–300.
- Kinoshita, M., H. Tobin, J. Ashi, G. Kimura, S. Lallement, E. J. Screaton, D. Curewitz, H. Masago, K. T. Moe, and Expedition 314/315/316 Scientists (Eds.) (2009a), *Proceedings of the Integrated Ocean Drilling Program*, 314/315/316, Site C0001, Ocean Drill. Program, College Station, Tex.
- Kinoshita, M., H. Tobin, J. Ashi, G. Kimura, S. Lallement, E. J. Screaton, D. Curewitz, H. Masago, K. T. Moe, and Expedition 314/315/316 Scientists (Eds.) (2009b), *Proceedings of the Integrated Ocean Drilling Program*, 314/315/316, Site C0002, Ocean Drill. Program, College Station, Tex.
- Kinoshita, M., H. Tobin, J. Ashi, G. Kimura, S. Lallement, E. J. Screaton, D. Curewitz, H. Masago, K. T. Moe, and Expedition 314/315/316 Scientists (Eds.) (2009c), *Proceedings of the Integrated Ocean Drilling Program*, 314/315/316, Site C0004, Ocean Drill. Program, College Station, Tex.
- Kinoshita, M., H. Tobin, J. Ashi, G. Kimura, S. Lallement, E. J. Screaton, D. Curewitz, H. Masago, K. T. Moe, and Expedition 314/315/316 Scientists (Eds.) (2009d), *Proceedings of the Integrated Ocean Drilling Program*, 314/315/316, Site C0006, Ocean Drill. Program, College Station, Tex.

- Kinoshita, M., H. Tobin, J. Ashi, G. Kimura, S. Lallement, E. J. Screaton, D. Curewitz, H. Masago, K. T. Moe, and Expedition 314/315/316 Scientists (Eds.) (2009e), *Proceedings of the Integrated Ocean Drilling Program, 314/315/316, Site C0007*, Ocean Drill. Program, College Station, Tex.
- Kitajima, H., and D. M. Saffer (2012), Elevated pore pressure and anomalously low stress in regions of low frequency earthquakes along the Nankai Trough subduction megathrust, *Geophys. Res. Lett.*, *39*, L23301, doi:10.1029/2012GL053793.
- Kopf, A., E. Araki, S. Toczko, and Expedition 332 Scientists (2011), *Proceedings of the Integrated Ocean Drilling Program, 332, Site C0002*, Ocean Drill. Program, College Station, Tex.
- Le Pichon, X., P. Henry, and S. Lallemand (1990), Water flow in the Barbados Accretionary Complex, *J. Geophys. Res.*, *95*(B6), 8945–8967.
- Moreno, M., C. Haberland, O. Oncken, A. Rietbrock, S. Angiboust, and O. Heidbach (2014), Locking of the Chile subduction zone controlled by fluid pressure before the 2010 earthquake, *Nat. Geosci.*, *7*(4), 292–296, doi:10.1038/ngeo2102.
- Ougier-Simonin, A., Y. Guéguen, J. Fortin, A. Schubnel, and F. Bouyer (2011), Permeability and elastic properties of cracked glass under pressure, *J. Geophys. Res.*, *116*, B07203, doi:10.1029/2010JB008077.
- Park, J.-O., T. Tsuru, S. Kodaira, P. R. Cummins, and Y. Kaneda (2002), Splay fault branching along the Nankai Subduction Zone, *Science*, *297*, 1157–1160.
- Paterson, M. S. (1990), Rock deformation experimentation, in *The Brittle-Ductile Transition in Rocks*, edited by A. G. Duba et al., vol. 56, pp. 187–194, AGU, Washington, D. C.
- Raimbourg, H., Y. Hamano, S. Saito, M. Kinoshita, and A. Kopf (2011), Acoustic and mechanical properties of Nankai accretionary prism core samples: Mechanical properties of Nankai samples, *Geochem. Geophys. Geosystems*, *12*, Q0AD10, doi:10.1029/2010GC003169.
- Raymer, L. L., E. R. Hunt, and J. S. Gardner (1980), An improved sonic transit time-to-porosity transform, in *SPWLA 21st Annual Logging Symposium*, Society of Petrophysicists and Well Log Analysts (SPWLA), Lafayette, Louisiana, pp. 1–13.
- Saffer, D., L. McNeill, T. Byrne, E. Araki, S. Toczko, N. Eguchi, K. Takahashi, and Expedition 319 Scientists (Eds.) (2010), *Proceedings of the Integrated Ocean Drilling Program, 319, Site C0011*, Integrated Ocean Drill. Program, College Station, Tex.
- Saffer, D. M. (2003), Pore pressure development and progressive dewatering in underthrust sediments at the Costa Rican subduction margin: Comparison with northern Barbados and Nankai, *J. Geophys. Res.*, *108*(B5), 2261, doi:10.1029/2002JB001787.
- Saffer, D. M., and B. A. Bekins (2006), An evaluation of factors influencing pore pressure in accretionary complexes: Implications for taper angle and wedge mechanics, *J. Geophys. Res.*, *111*, B04101, doi:10.1029/2005JB003990.
- Saito, S., M. B. Underwood, Y. Kubo, and Expedition 322 Scientists (Eds.) (2010a), *Proceedings of the Integrated Ocean Drilling Program, 322, Site C0011*, Ocean Drill. Program, College Station, Tex.
- Saito, S., M. B. Underwood, Y. Kubo, and Expedition 322 Scientists (Eds.) (2010b), *Proceedings of the Integrated Ocean Drilling Program, 322, Site C0012*, Ocean Drill. Program, College Station, Tex.
- Spinelli, G. A., P. S. Mozley, H. J. Tobin, M. B. Underwood, N. W. Hoffman, and G. M. Bellew (2007), Diagenesis, sediment strength, and pore collapse in sediment approaching the Nankai Trough subduction zone, *Geol. Soc. Am. Bull.*, *119*(3–4), 377–390.
- Underwood, M. B., N. Basu, J. Steurer, and K. Udas (2003), 5. Data report: Normalization factors for semiquantitative X-Ray diffraction analysis, with application to DSDP site 297, Shikoku Basin, *Proc. Ocean Drill. Program Sci. Results*, *190/196*, 28.
- Wyllie, M. R. J., A. R. Gregory, and G. H. F. Gardner (1958), An experimental investigation of factors affecting elastic wave velocities in porous media, *Geophysics*, *23*, 400.
- Yamamoto, Y. (2006), Systematic variation of shear-induced physical properties and fabrics in the Miura-Boso accretionary prism: The earliest processes during off-scraping, *Earth Planet. Sci. Lett.*, *244*(1–2), 270–284, doi:10.1016/j.epsl.2006.01.049.
- Yamamoto, Y., H. Mukoyoshi, and Y. Ogawa (2005), Structural characteristics of shallowly buried accretionary prism: Rapidly uplifted Neogene accreted sediments on the Miura-Boso Peninsula, central Japan, *Tectonics*, *24*, TC5008, doi:10.1029/2005TC001823.